Tectonophysics 769 (2019) 228166

Contents lists available at ScienceDirect

Tectonophysics

journal homepage: www.elsevier.com/locate/tecto

Synthesizing sea surface height change including seismic waves and tsunami using a dynamic rupture scenario of anticipated Nankai trough earthquakes

Tatsuhiko Saito[a,*], Toshitaka Baba[b], Daisuke Inazu[c], Shunsuke Takemura[a,1], Eiichi Fukuyama[a]

[a] National Research Institute for Earth Science and Disaster Resilience, Tsukuba, Ibaraki, Japan
[b] Graduate School of Technology, Industrial and Social Sciences, Tokushima University, Tokushima, Japan
[c] Department of Marine Resources and Energy, Tokyo University of Marine Science and Technology, Tokyo, Japan

ARTICLE INFO

Keywords:
Seismic wave
Tsunami
Earthquake rupture
Sea surface displacement

ABSTRACT

The development of offshore observation technology will provide researchers with tsunami records from within an earthquake focal area, but this will create new problems. Because seismic waves coexist with tsunami inside a focal area, the seismic waves could act as noise for the tsunami signal. This study shows an efficient method to calculate sea surface height change caused by an earthquake including both seismic waves and tsunami. Simulation results indicate that seismic waves overlap with tsunami; both affect the change in sea surface height although most previous tsunami studies have neglected the contribution of seismic waves. We also numerically simulated the sea-surface displacement wavefield and hypothesized results for an anticipated rupture scenario of a huge earthquake that may possibly occur in the Nankai Trough, Japan. The synthesized record could be used to evaluate the performance of a real-time tsunami prediction method. Additionally, we discussed the similarity and difference between two kinds of tsunami waveforms: the displacement of the sea surface and the pressure change at the sea bottom. Although seismic waves appeared in both waveforms, the contribution of seismic waves was lower in the displacement at the sea surface than in the pressure change at the sea bottom.

1. Introduction

The development of observation technology has greatly promoted our understanding of tsunami characteristics. In the past, tsunami records used for waveform analyses were mainly obtained by tide gauges. However, tide gauges detect tsunamis only at coasts or in very shallow seas. These records are considerably affected by the specific geometry of each harbor and bay (e.g., Namegaya et al., 2009; Hayashi, 2010). However, tsunami records observed at deep ocean sites are usually free from site effects, which makes it possible to investigate the details of tsunami propagation and the source process (e.g., Inazu and Saito, 2014; Tsushima and Ohta, 2014; Kubota et al., 2018a). In particular, tsunamis with short wavelengths showing such dispersion were clearly recorded in the deep ocean (e.g., González and Kulikov, 1993; Saito et al., 2010b). Nonetheless, we should note that waves with short wavelengths are not reproduced by the long wave equation that was often used for simulating the tide gauge records. Dipersive approaches such as the Boussinesq equation are necessary for modeling short wavelength tsunami in deep oceans (e.g., Tanioka, 2000; Saito et al., 2010a; Kirby et al., 2013; Miyoshi et al., 2015; Dettmer et al., 2016; Baba et al., 2017). This clearly indicates that we need to use an appropriate theory depending on the observation situation.

In most cases, tsunami observation in deep seas has been conducted far from the tsunami source. Recently, observations have been increasing within eathquake rutpure areas. In eastern Japan, numerous sensors are densely deployed in a wide area where extensive tsunamigenic earthquakes could possibly occur in future (e.g., Maeda et al., 2015; Yamamoto et al., 2016; Kubota et al., 2018b). This situation is essentially different from the case where sensors were located far from the source. When the observation site is distant from the source, the tsunami arrives much later than seismic waves because tsunamis propagate much slower than seismic waves. Hence, the tsunami signal is separately recorded from the seismic signal in a waveform record. However, if the observation point is inside the focal area, the seismic waves overlap with the tsunami. We therefore cannot specifically detect tsunami signals because of contamination by seismic waves. In order to analyze the tsunami signal overlapped with seismic waves, we need to know how the seismic wave appears in the record. It is therefore important to simulate records including both tsunami and seismic waves.

Currently two kinds of sensors are predominantly used to record

* Corresponding author.
E-mail address: saito-ta@bosai.go.jp (T. Saito).
[1] Present at Earthquake Research Institute, The University of Tokyo, Tokyo, Japan.

https://doi.org/10.1016/j.tecto.2019.228166
Received 15 January 2019; Received in revised form 18 April 2019; Accepted 26 July 2019
Available online 29 July 2019

tsunami signals. One is an ocean-bottom pressure gauge that measures the pressure change at the seabed. Some studies developed a method for rapid tsunami prediction near coastlines by analyzing pressure changes (e.g., Titov et al., 2005; Tang et al., 2009; Tsushima et al., 2009; Gusman et al., 2016; Yang et al., 2019). Recently Saito and Tsushima (2016) investigated how seismic waves influence the pressure changes and the effects of these on rapid tsunami source estimation. Another sensor is real-time kinematic (RTK) GPS that measures the displacement at the sea surface (e.g., Kato et al., 2000). Foster et al. (2012) reported that a kinematic GPS deployed on a ship detected an off-shore tsunami of 0.1 m due to the 2010 Maule, Chile, earthquake. Recent studies have developed a method for a real time tsunami source estimation by using the displacement at the sea surface (Inazu et al., 2016; Mulia et al., 2017). These studies illustrated that the GPS gauges located upon cargo ships are potentially available to measure the displacement at the sea surface and that this data can be used for rapid source estimation. However, the contribution of seismic waves to the sea surface displacement has been neglected. It is important to understand how seismic waves and tsunami each contribute to the sea surface displacement.

There are a few established approaches for synthesizing the displacement caused by an earthquake. The normal mode theory is used for the wavefield in the simple 1-D structure constituted from the sea layer and subsurface layers (e.g., Ward, 1980), but these waveforms might be too simple to compare with observed records. Numerical simulations of the finite difference method can take a realistic bathymetry into account (e.g., Maeda et al., 2013; Maeda and Furumura, 2013; Lotto and Dunham, 2015).

This study shows an alternative efficient numerical method to synthesize displacement at the sea surface caused by an earthquake including both seismic waves and tsunami. Section 2 illustrates our method to synthesize the sea-surface height change. Section 3 shows the example of the sea surface height change caused by an earthquake in a simple case to demonstrate the fundamental nature of seismic waves and tsunami. In Section 4, by integrating a dynamic earthquake rupture model with our numerical method, we synthesized hypothetical records for a scenario based upon the anticipated huge Nankai Trough earthquake. By using the synthesized scenario records, we evaluated an automated tsunami source estimation method. Section 5 discusses the merit and detriment of our synthesizing method. We also briefly mention the intrinsic difference between the seismic-wave contribution to sea surface height and sea bottom pressure changes.

2. A theory for sea-surface height change

When an earthquake occurs beneath the sea, displacement of the sea floor due to the earthquake uplifts the sea surface (Fig. 1a). The raised sea surface then collapses due to gravity and a massive amount of seawater is displaced in a horizontal direction. The displacement propagates as tsunami (Fig. 1b). This process is theoretically investigated based on water wave theory (e.g., Takahashi, 1942; Kajiura, 1963; Kervella et al., 2007; Saito, 2013; Saito, 2019). The theory suggests that the generation process is basically described without gravity, whereas tsunami propagation is due to gravity as restoring force. Most past studies implicitly assumed this idea and neglected gravity when calculating the initial tsunami-height distribution (e.g., Satake, 2015; Heidarzadeh et al., 2017). This study also follows this idea and employs a two-step method (Saito, 2019) to calculate the evolution of the displacement as shown below.

2.1. Linear seismic wave simulation

In order to include the contribution of seismic waves in tsunami generation, we use the equation of motion for the whole location including sea and crust as

$$\rho \frac{\partial v_i(\mathbf{x}, t)}{\partial t} = \tau_{ij,j} + f_i, \tag{1}$$

where ρ is the density of the medium (sea and crust), v_i is velocity field, τ_{ij} is the stress field, and f_i is the body force distribution that is equivalent to a fault motion. We represent a finite earthquake fault as a set of numerous point dislocation sources. The constitutive relation of the elastic medium:

$$\frac{\partial \tau_{ij}}{\partial t} = \lambda \delta_{ij} v_{k,k} + 2\mu (v_{i,j} + v_{j,i}), \tag{2}$$

is used where λ and μ are Lamé's constants.

Note that the equation of motion (Eq. (1)) does not include gravity. Therefore, the calculated sea surface shows permanent deformation over the focal region. We then use the vertical velocity at the sea surface $v_z(x, y, z_{\mathrm{sur}}, t)$, where z_{sur} represents the sea surface, as an input in the following tsunami simulation.

2.2. Nonlinear tsunami simulation

At the second step, we conduct a tsunami propagation simulation in order to simulate the time evolution of sea surface displacement due to gravity. We use nonlinear long wave tsunami equations:

$$\frac{\partial \eta}{\partial t} + \frac{\partial}{\partial x}[(h + \eta) v_x^{\mathrm{av}}] + \frac{\partial}{\partial y}[(h + \eta) v_y^{\mathrm{av}}] = 0, \tag{3}$$

$$\frac{\partial v_x^{\mathrm{av}}}{\partial t} + v_x^{\mathrm{av}} \frac{\partial v_x^{\mathrm{av}}}{\partial x} + v_y^{\mathrm{av}} \frac{\partial v_x^{\mathrm{av}}}{\partial y} + g_0 \frac{\partial \eta}{\partial x} = 0, \tag{4}$$

and

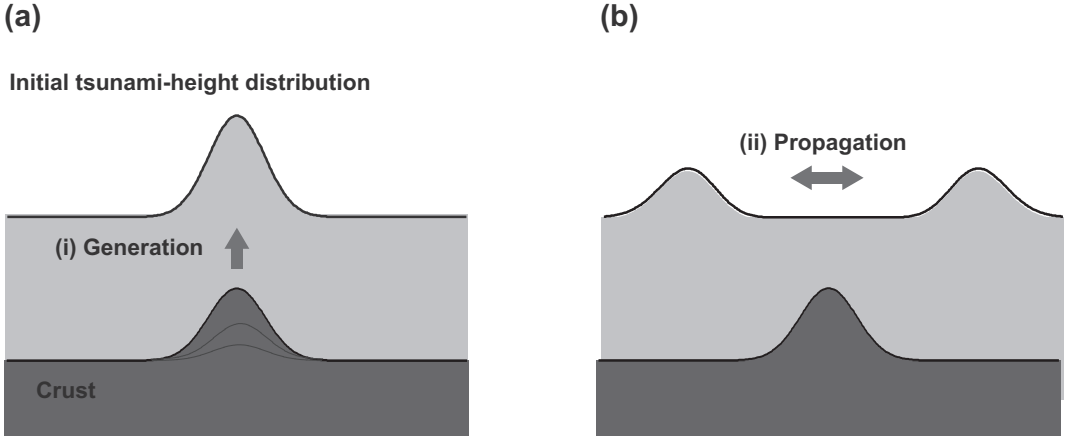

Fig. 1. A schematic illustration of (a) tsunami generation and (b) propagation.

$$\frac{\partial v_y^{av}}{\partial t} + v_x^{av}\frac{\partial v_y^{av}}{\partial x} + v_y^{av}\frac{\partial v_y^{av}}{\partial y} + g_0\frac{\partial \eta}{\partial y} = 0, \quad (5)$$

where η is vertical displacement at the sea surface, h is the sea depth, ${v_x}^{av}$ and ${v_y}^{av}$ represent horizontal velocity averaged over the sea depth, and g_0 is the gravitational acceleration.

At time $t_i = i\Delta t$, sea surface height is incremented by $\Delta\eta\ (x,y,t)$ as

$$\eta(x,y,t_i) = \eta^*(x,y,t_i) + \Delta\eta(x,y,t_i) \quad (6)$$

where $\eta^*(x,y,t_i)$ is the tsunami height distribution calculated from the tsunami height and velocities at the previous time $t = t_{i-1}$ based on Eqs. (3), (4), and (5). The increment of the sea-surface height $\Delta\eta\ (x,y,t_i)$ is produced from vertical velocity at the sea surface $v_z(x,y,z_{sur},t_i)$ numerically calculated by the seismic wave simulation:

$$\Delta\eta(x,y,t_i) = v_z(x,y,z_{sur},t_i)\Delta t. \quad (7)$$

Eqs. (3), (4), (5) and (6) capture the surface-height evolution caused by elasticity and gravity as restoring force.

2.3. Difference from the method proposed by Saito and Tsushima (2016)

Saito and Tsushima (2016) proposed another two-step method for the ocean-bottom pressure change. The methods proposed in this study and that in Saito and Tsushima (2016) look similar at first glance. However, there is an intrinsic difference between them. Saito and Tsushima (2016) calculated the pressure change while the present study calculates the surface displacement.

For pressure change, the signal would be decomposed into two components without any overlap between the two components in a linear system: one is related to gravity and the other is independent of gravity but due to fluid motion. However, for the sea surface displacement, the sea surface height cannot be simply decomposed into two parts. Hence, we use Eqs. (6) and (7) to include the contributions from elasticity and gravity. Using Eqs. (6) and (7), this study continuously connects the wavefield dominated by seismic waves for short elapsed time and small time scale (Saito, 2017) to the wavefield dominated by tsunami for long elapsed time and long time scale.

3. Simulations using kinematic sources: a simple case

3.1. Simulation setting

In order to illustrate fundamental features of seismic waves and tsunami, this section employs a simple model: a 2-D layered structure consisting of sea and crust (Fig. 2). Sea layer is characterized by *P*-wave velocity of $V_P = 1.5$ km/s, *S*-wave velocity of $V_S = 0.0$ km/s, and density of $\rho = 1.0 \times 10^3$ kg/m^3 and the crust is characterized by $V_P = 6.92$ km/s, $V_S = 4.0$ km/s, and $\rho = 2.8 \times 10^3$ kg/m^3. At the boundary between liquid and air layers, traction-free condition is set. The sea depth is set as $h_0 = 4$ km. An earthquake fault represented as 100 km long with 15 degrees dip is embedded in the crust. The shallowest part of the fault is located 5 km below the sea floor. A uniform slip of $d_0 = 1$ m on the fault is assumed. The slip rate function is given by the Gaussian function as,

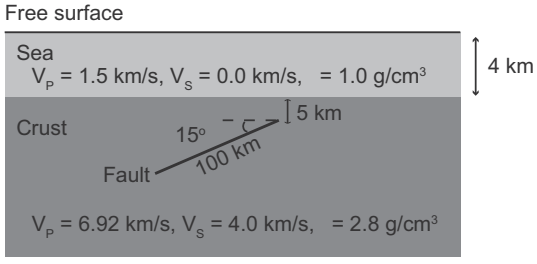

Fig. 2. A layered structure consisting of sea and crust.

$$f(t) = \frac{1}{\sqrt{\pi}}\frac{4}{t_c}\exp\left[-\left(\frac{t-t_0}{t_c/4}\right)^2\right] \quad (8)$$

where the parameter t_0 (= 60 s) represents the time of the peak slip rate and t_c represents rise time.

The two-step simulation explained in Section 2 is conducted in the 2-D space. At the first step, we conducted seismic wave simulation using the finite difference method with the second order in space and time (e.g., Saito, 2017). Note that we used the second-order approximation of finite difference in space (the grid spacing is 0.2 km), because the fourth order or higher order approximation in space is not appropriate to represent fluid-solid/fluid-air boundaries (e.g., Nakamura et al., 2012; Takemura et al., 2015). Using the second-order approximation for the finite difference operation in time with the time step of 0.01 s (Ohminato and Chouet, 1997), this study focuses on seismic waves whose period is longer than about a few seconds. In the boundary between the sea and crust, the density is given by the arithmetic average as effective medium parameters (Nakamura et al., 2012).

3.2. Tsunami simulation including seismic waves

Fig. 3 shows the simulated results for a source duration $t_c = 10$ s in a sea depth of $h_0 = 4$ km. Vertical displacement at the sea surface is plotted in blue and vertical displacement of the sea floor is plotted in black. These plots lie in the upper panel. The velocity distribution (vertical component) is displayed in lower panel for different elapsed times. We see a Rayleigh wave propagating towards the right along the sea surface and the sea bottom (Fig. 3a–c). Ocean acoustic waves (or *P*-waves trapped within the sea layer) also appear. Note that sea surface height distribution and the sea bottom height distribution are not in agreement for all the elapsed times. This difference is due to the existence of seismic waves. The sea surface displacement remains as a permanent deformation (Fig. 3d).

The second step involved conducting tsunami simulation by using the sea surface velocity calculated by the seismic wave simulation. Fig. 4 shows the temporal change in the sea-surface height distribution calculated by the tsunami simulation and the sea-bottom deformation calculated by the seismic simulation. Because the tsunami equations (Eqs. (4)–(6)) include gravity, the sea surface elevation collapses and propagates as tsunami. At the elapsed times of 200 and 800 s, tsunami propagation is clearly recognized. The peak height is located at 30 and 150 km at times equal to 200 s and 800 s. The velocity is ~0.2 km/s. This is also predicted by the long wavelength theory for tsunami as $\sqrt{g_0 h_0}$~0.2 km/s for $h_0 = 4$ km. With careful scrutiny, we can see a slight difference between the sea surface height in Fig. 4b and that in Fig. 3b at the elapsed time of 80 s. This difference is due to gravity. A dashed line indicates the maximum sea-surface height distribution. The peak of the maximum height distribution is ~0.6 m.

3.3. Tsunami simulation excluding seismic waves

In order to clarify the contribution of seismic waves to sea surface height distribution, we conducted tsunami simulation without seismic waves. First, we calculated the permanent sea bottom vertical displacement caused by the earthquake faulting in a homogeneous half space. We solved the equilibrium equation by using the code of Okada (1985). Then we calculated the sea surface height distribution caused by the sea bottom displacement based on the analytical solution of the incompressible fluid theory (Kajiura, 1963). Note that Saito (2017) compared the permanent vertical displacement at the sea surface calculated by elastic dynamics with compressible sea water and that calculated by fluid dynamics with incompressible sea water to confirm that these two permanent vertical displacement distributions were almost identical. This is because the shear strain dominates over the volumetric strain in the sea water. We set the sea surface height distribution calculated by assuming an incompressible fluid as $\eta_0(x,z_{sur})H$

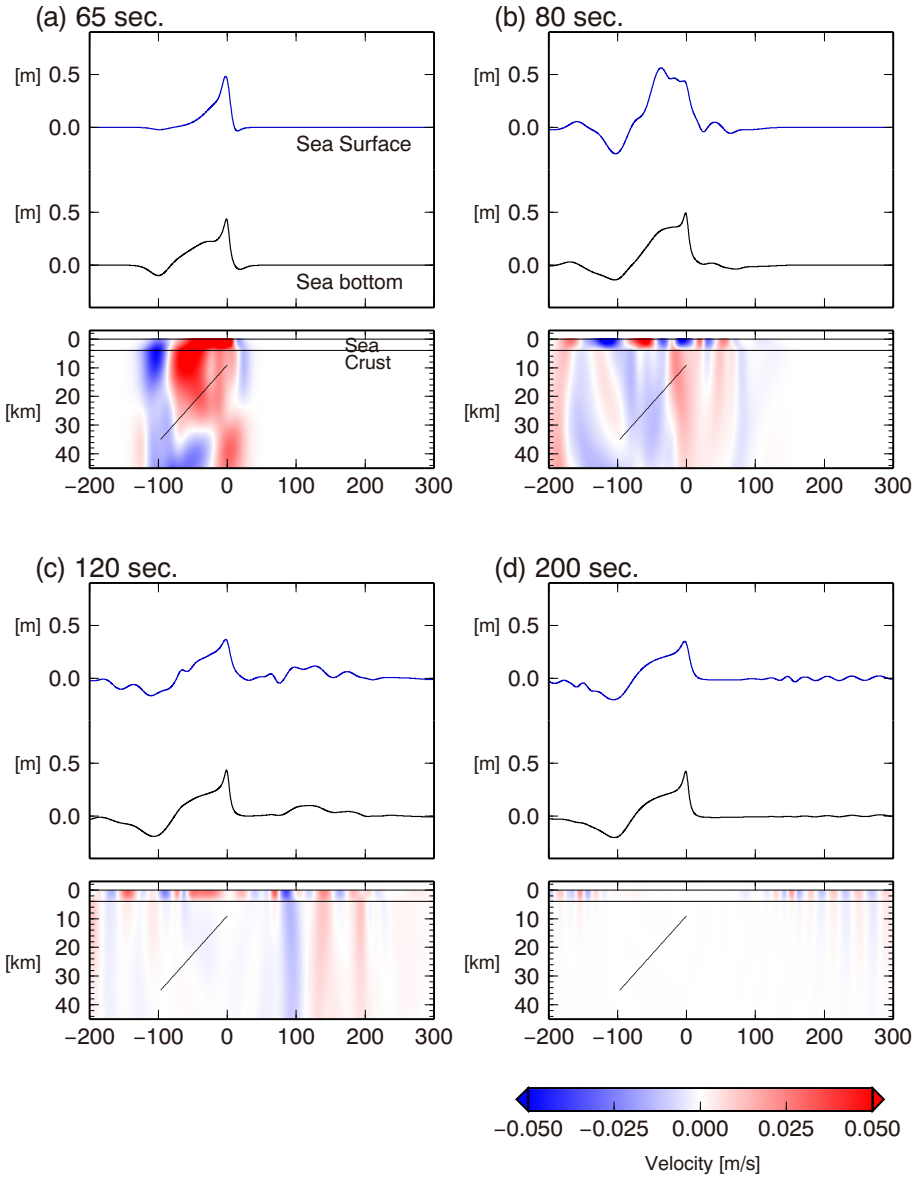

Fig. 3. Results of seismic wave simulations with the source duration given by t_c = 10 s for the various elapsed times: (a) 65 s; (b) 80 s; (c) 120 s; and (d) 200 s. Vertical-displacement distributions at the sea surface (blue) and at the sea bottom (black) are plotted in the upper bin. Vertical-velocity distribution in the vertical cross section is displayed with a color map in the lower bin. The sea depth is 4 km ($0 < z < 4$ km). The black line in the crust indicates the earthquake fault. (For interpretation of the references to color in this figure legend, the reader is referred to the web version of this article.)

(t). This is the response of the fault slip given by $d_0H(t)$ (d_0 = 1 m) where $H(t)$ is the step function. Since the sea surface change caused by the earthquake is proportional to the fault slip in this study (a linear problem), we calculated the sea surface vertical velocity $v_z(x, z_{sur}, t)$ for the slip rate function $f(t)$ (Eq. (8)) by multiplying the slip rate function (Eq. (8)) with the sea surface displacement as $v_z(x, z_{sur}, t) = \eta_0(x, z_{sur})f(t)$. This vertical velocity does not include seismic waves. We simulated the tsunami propagation using this sea surface velocity in Eqs. (6) and (7).

Fig. 5 shows the simulation results without seismic waves. The sea surface height distribution in Fig. 5 is much smoother than found in Fig. 4 in the time window between 65 and 120 s because of the absence of seismic waves. As a result, the maximum height at the sea surface (~0.3 m) is smaller than that in Fig. 4. However, we should note that at later times (for example at the time of 800 s) the sea-surface height distributions at Figs. 4f and 5f are almost identical.

Fig. 6 compares sea-surface displacement both including seismic waves (red) and without seismic waves (gray). At 65 s, there is a significant difference between the sea surface height distributions. At 800 s we see excellent agreement between the two lines. This is because the seismic waves no longer exist in the simulation region and only the tsunami remains. This indicates that the tsunami is almost independent of seismic waves. In other words, we can simulate tsunami appropriately without considering seismic waves.

Fig. 7a shows the temporal change in the sea surface height at $x = -50$ km. A red line indicates the sea surface height change when the earthquake rupture is characterized by t_c = 10 s, which shows large-amplitude and high-frequency oscillation between ~60 s and ~200 s. The dominant period of oscillation is ~10 s. In comparison, we plot the sea surface height change calculated without seismic waves (gray line). There is a significant difference between the two waveforms, particularly between the high-frequency components (~10 s). Also, the maximum height is ~0.5 m when including seismic waves whereas it is ~0.15 m when seismic waves are not considered. We applied a low-pass filter (the cut-off period is 60 s) to the waveform in order to remove the high-frequency seismic waves (Fig. 7b). The cut-off period of 60 s was

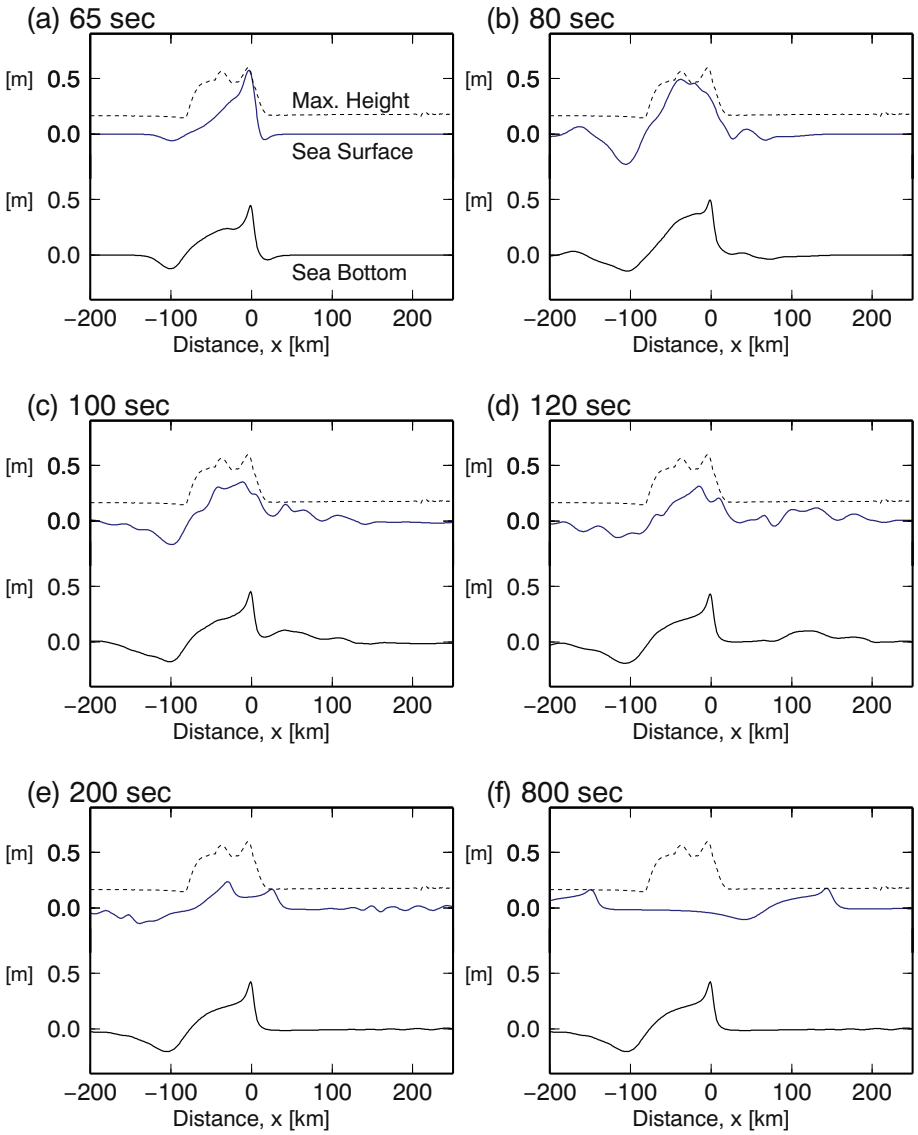

Fig. 4. Results of tsunami simulation in the case the source duration is given by $t_c = 10$ s. Vertical-displacement distributions at the sea surface (blue) and at the sea bottom (black) are plotted in the upper bin. Dashed lines indicate the maximum sea-surface height distribution. (For interpretation of the references to color in this figure legend, the reader is referred to the web version of this article.)

set by Tsushima et al. (2012) to remove the high frequency noise but to keep the tsunami signal in actual observed records. Fig. 7b shows that the low-pass filter considerably reduced the high-frequency component, although we still found a small difference between the two waveforms at the elapsed time ~100 s. This indicates that we cannot completely remove the seismic waves with the low pass filter.

4. Simulations using dynamic rupture model and realistic bathymetry data

In this section, we simulated sea surface displacement using a more realistic model. A large earthquake that is anticipated to occur in the Nankai Trough, southwestern Japan, is simulated as an example.

4.1. A rupture model

Along the Nankai trough, southwestern Japan (Fig. 8), the Philippine Sea Plate subducts beneath the Eurasian Plate at a rate of 2–6 cm per year (e.g., Seno et al., 1993). Great earthquakes (M ~ 8) have occurred repeatedly along the plate interface with a recurrence interval on the order of 100 years (e.g., Kumagai, 1996; Ishibashi, 2004). The 1944 Tonankai (M 7.9) and the 1946 Nankai (M 8.0) earthquakes caused serious tsunami damage along the Pacific coast of southwestern, Japan. The 1707 Hoei earthquake is believed to have ruptured the whole region from Hyuganada to the Tokai area (e.g., Furumura et al., 2011). Such huge earthquakes generated strong ground motion and tsunami, which caused serious damage throughout this region (e.g., Furumura and Saito, 2009; Kim et al., 2016).

We used an earthquake scenario proposed by Hok et al. (2011). The rupture model was constructed based on the friction law established in laboratory experiments and the slip deficit distribution estimated using geodetic-data analysis. Fig. 9 shows the evolution of the slip distribution for the 1946 Nankai-like earthquake scenario. Fig. 10a shows the temporal change in potency $P(t)$ calculated as

$$P(t) = \iint_S d(\xi, t) dS(\xi) \tag{9}$$

where $d(\xi, t)$ is the dislocation on the fault area $S(\xi)$, and Fig. 10b shows the potency rate. The seismic wave amplitude is proportional to the potency rate rather than the potency itself (e.g., Aki and Richards, 2002). Fig. 10c shows the spectral amplitude of the potency rate. The

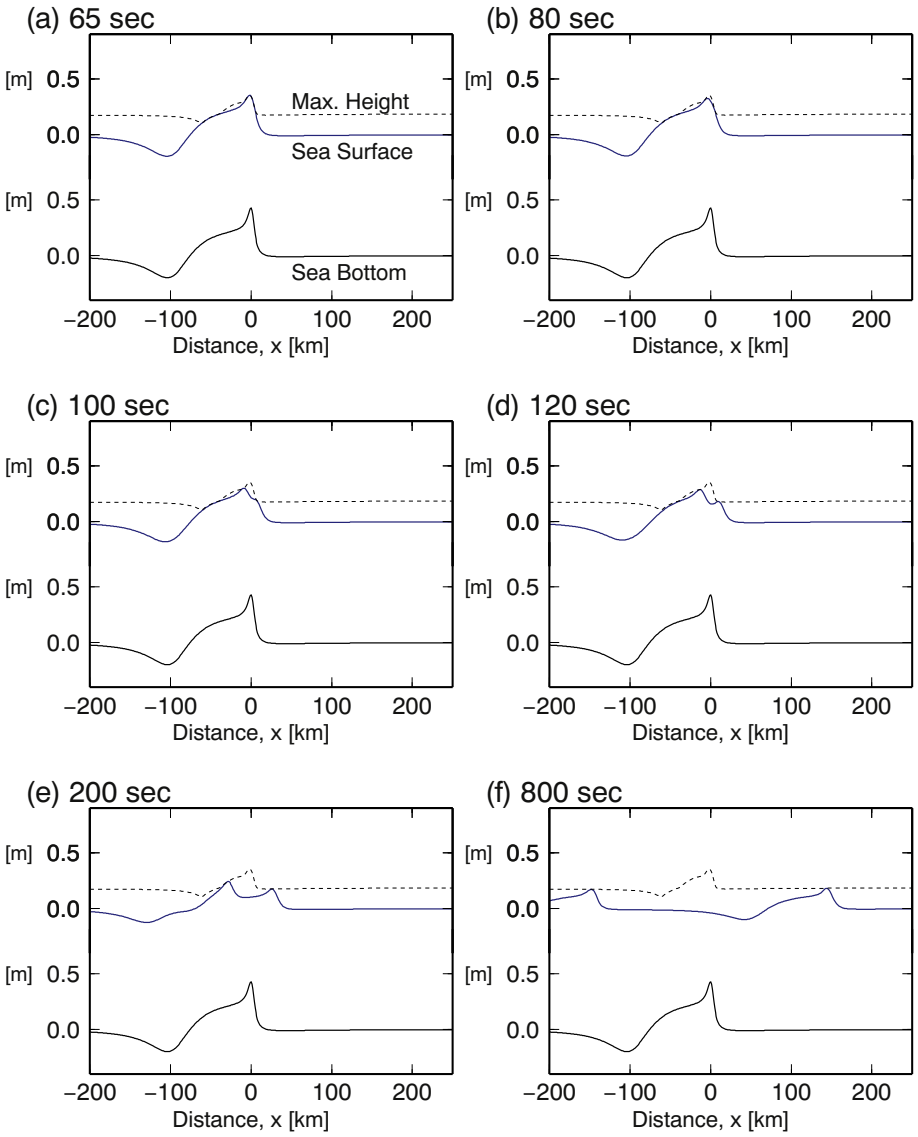

Fig. 5. Results of a tsunami simulation without seismic waves. Vertical-displacement distributions at the sea surface (blue) and at the sea bottom (black) are plotted in the upper bin. Dashed lines indicate the maximum sea surface height distribution. (For interpretation of the references to color in this figure legend, the reader is referred to the web version of this article.)

high frequency (> 0.01 Hz) components decrease rapidly with increasing frequency. The rupture starts in the area adjacent to cape Shiono and propagates westward (local names shown in Fig. 8). At the time of 80 s, the rupture reaches nearby cape Muroto and the potency rate (or moment rate) reaches a peak (Fig. 10b). A large slip of greater than ~6 m appears off cape Muroto. The rupture ends at the time of 120 s. The final value of the potency is ~130 km^3 corresponding to M_W 8.4 ($M_0 = 5.8 \times 10^{21}$ N m) where the rigidity is $\mu = 45$ GPa.

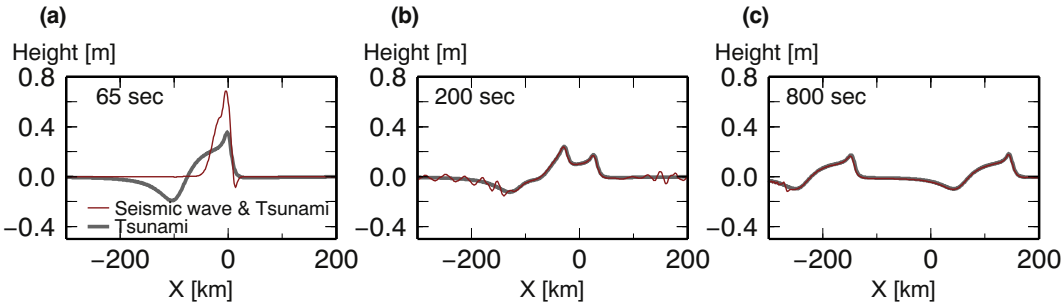

Fig. 6. Sea-surface height distributions for various elapsed times: (a) 65 s, (b) 200 s, and (c) 800 s from the origin time. Red lines are the simulation results including both seismic waves and tsunami. Gray lines are the results including only tsunami. (For interpretation of the references to color in this figure legend, the reader is referred to the web version of this article.)

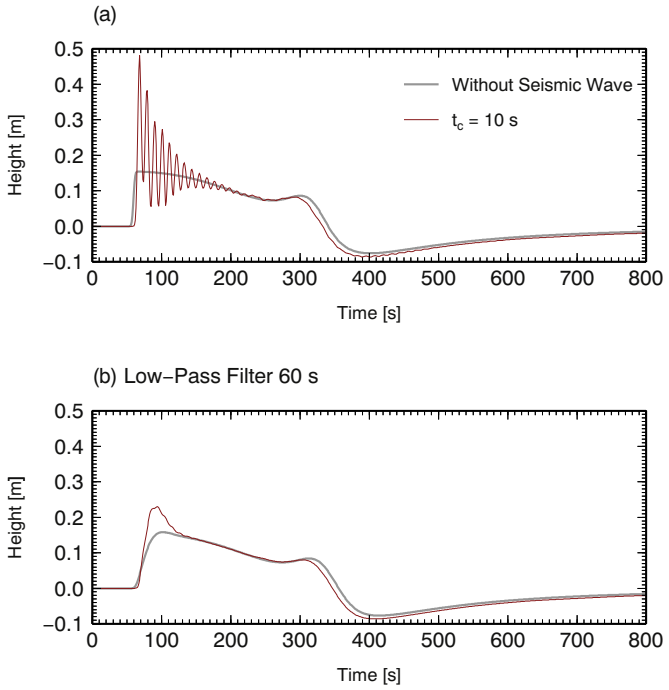

Fig. 7. (a) Temporal change in sea surface height inside the focal area ($x = -50$ km in Fig. 3) for the case of source duration $t_c = 10$ s. Comparison of a synthesis including seismic wave contribution (red line) and a synthesis without seismic wave contribution (gray line). (b) Temporal change in sea-surface height after applying a low-pass filter with a cutoff period of 60 s. (For interpretation of the references to color in this figure legend, the reader is referred to the web version of this article.)

4.2. Seismic wave simulation

Hok et al. (2011) used 13,385 triangular elements to represent a dynamic rupture. The size of each triangular element changes according to the location. The area of each triangular element varies according to the dip of the area and is ~20 km^2. By representing each triangular element as a point source moment tensor, we represent the spatial and temporal distribution of the dislocation in the 3-D seismic wave propagation simulation.

In the seismic wave simulation, we used a layered subsurface structure (Table 1) with topography and bathymetry. We used ETOPO1 for the topography and bathymetry data (Amante and Eakins, 2009). The elastic wave velocities and density are listed in Table 1 (e.g., Dziewonski and Anderson, 1981). Lamé's constants are given by $\lambda = \rho(V_P{}^2 - 2V_S{}^2)$ and $\mu = \rho V_S{}^2$. The attenuation was included in the whole space by the method of Graves (1996) with $Q = 600$ for the wave period of 1 s. The simulation region is shown in Fig. 8. The region was discretized by the horizontal grid spacing of 0.5 km and the vertical grid spacing of 0.25 km. Our simulations calculate seismic waves for wavelengths longer than 20 km (0.5 km × 40 grid spacing) without significant numerical dispersion. This corresponds to wave periods longer than ~7 s for an S-wave velocity of 3.2 km/s. We used 1800 (EW direction) × 1600 (NS direction) × 796 (vertical direction) grids to represent the simulation region. We numerically solved the equations of motion by the finite difference method with the time step of $\Delta t = 0.01$ s for 600 s (60,000 steps).

Fig. 11 shows snapshots of vertical displacement on the free surface (sea surface in sea and ground surface in land) calculated by the simulation. Rayleigh wave propagation along the dip direction is recognized at the elapsed time from 30 s to 150 s (marked by R). At 150 s, a large-amplitude Rayleigh wave propagates towards the southwest because of the rupture directivity. The vertical displacement remains permanently inside the focal area.

4.3. Tsunami simulation

Tsunami simulation is conducted by using the result of seismic wave simulation: the change in the sea surface height $v_z(x,y,z_{sur},t_i)\Delta t$ is added to the sea surface height during the time from t_i to $t_i + \Delta t$ based on Eqs. (6) and (7). We also included the change in the bathymetry as

$$h(x,y,t_i) = h(x,y,t_{i-1}) - v_z(x,y,z_{bot},t_i)\Delta t \quad (10)$$

where $v_z(x,y,z_{bot},t_i)$ is the vertical velocity at the sea floor, calculated by the seismic wave simulation. We simulate the spatial and time evolution of sea surface height change $\eta(x,y,t)$ due to gravity and the inundation based on the nonlinear long-wave equations (Eqs. (3), (4), and (5)) and a moving boundary condition.

In order to simulate the tsunami near coastlines, we need to use finer grid spacing for the bathymetric and topographic data. The bathymetry data is compiled from the General Bathymetric Chart of the Oceans, the M7000 series of digital bathymetric contour maps (a compilation of all locally available bathymetric maps of Japanese coastal waters) provided by the Japan Hydrographic Association, and Lidar surveys (remotely sensed laser reflection data) collected along the Japanese coast by the Geospatial Information Authority of Japan. We used six nested grids: the grid spacings are 18 arcsec, 6 arcsec 2 arcsec, 2/3 arcsec, 2/9 arcsec and 2/27 arcsec (~2 m). We numerically calculated nonlinear tsunami equations (Eqs. (3), (4), and (5)) for the propagation of a tsunami for 3 h with a time step of 0.025 s based on the finite difference method using JAGURS (Baba et al., 2016).

Fig. 12 shows the simulated vertical displacement at the sea surface at elapsed times of 1, 10, 30 and 60 min. At the time of 1 min, the earthquake rupture is propagating westward. High sea-surface height (> 0.5 m) is recognized off cape Muroto and cape Shiono (local names are shown in Fig. 8). At the elapsed times of 10–30 min, the tsunami approaches and arrives at coasts around the Nankai and the Tonankai regions. At the time of 60 min, the tsunami reaches the coast along Kyushu.

Fig. 13 shows the temporal change in the vertical displacement on the sea surface at each hypothetical station (open triangles in Fig. 14a). Those hypothesized stations were originally set by Inazu et al. (2016). Blue lines in Fig. 13b show the waveforms of the rupture scenario shown in Fig. 9. As a comparison, gray lines indicate the waveforms of the vertical displacement distribution at the elapsed time of 600 s (we consider this as the permanent sea-surface displacement caused by the earthquake if there is no gravity); used as the initial tsunami height distribution. There is a difference between the waveforms of blue and gray lines, which was mainly because of the effect of earthquake rupture evolution, not seismic waves. Small differences due to the seismic waves were recognized at waveforms t0015 and KME20 at the elapsed time of 50 s. The contribution of the seismic waves was minor in the sea-surface displacement in this simulation. This is because that the source does not contain much high-frequency energy (the corner frequency is ~0.01 Hz in Fig. 10c).

4.4. Inundation simulation

It was difficult to simulate the inundation including the seismic waves because the time scale of the high-frequency ground oscillation and the tsunami inundation are considerably different. If we include the seismic waves in the inundation simulation, the sea-bottom oscillation (vertical displacement at the sea bottom) is possibly greater than the sea depth in some places. This is physically inconsistent because it can break the volume conservation of the water, which was assumed in the tsunami simulation. Hence, we calculated the tsunami inundation without seismic wave propagation.

We should note that the tsunami is almost independent of seismic waves as we showed in Fig. 6. Hence, we can calculate the inundation correctly even if we neglect seismic waves (or transient sea bottom motion). However, the permanent displacement is not negligible in the

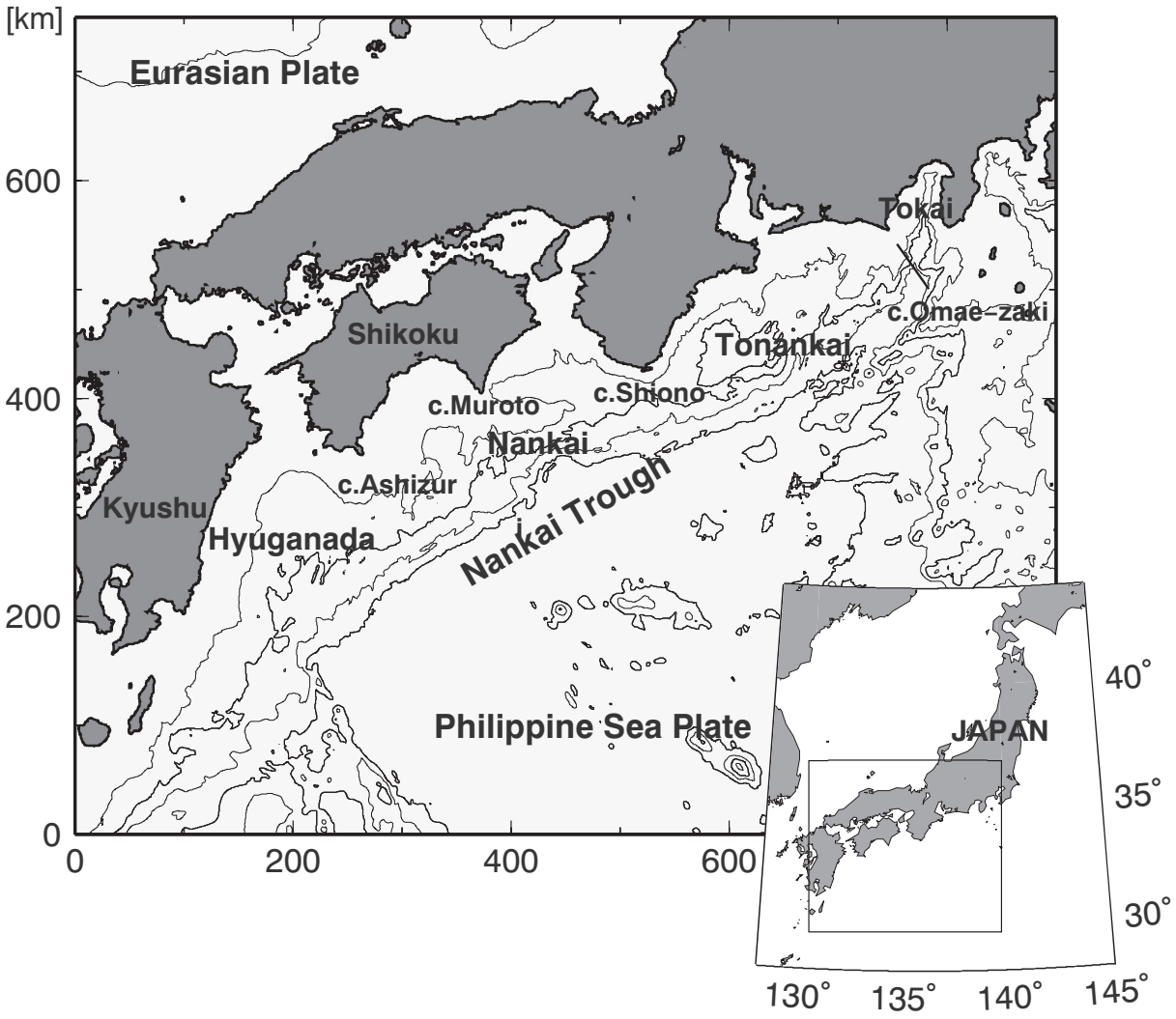

Fig. 8. Map of southwest Japan. Around the Nankai trough, the Philippine sea plate subducts underneath the Eurasian Plate. The region is divided into four areas: Hyuganada, Nankai, Tonankai, and the Tokai region.

inundation. We simulated the inundation including the permanent displacement by starting the tsunami simulation after the topography/bathymetry is displaced by the permanent displacement due to the earthquake.

Fig. 14a shows topography around the city Kochi, the largest city in the southern part of Shikoku. Fig. 14b shows the inundated areas in Kochi city caused by this earthquake scenario. The most striking feature of this result is that major inundation occurs at areas ~6 km from the coastline. This is due to the tsunami running up along the rivers. A simulation with a 500 m grid spacing cannot correctly describe the geometry of the rivers. Our high-resolution tsunami simulation (with ~6 m grid spacing) can correctly simulate the tsunami runup through the rivers. Tsunami propagation is very slow in the rivers. It takes > 1 h from the earthquake occurrence until the inundation height exceeds 0.3 m (Fig. 14c).

4.5. Testing real-time tsunami monitoring

By using our synthesized records of the huge earthquake, we evaluated the capability of a real time tsunami source estimation method using the vertical displacement at the sea surface (Inazu et al., 2016). Fig. 15a shows the locations of 92 hypothetical observation points used in the numerical experiment. The initial tsunami height distribution is represented by 376 sea-surface height elements. Each sea-surface element is given by Gaussian function ($\eta_{0j} = a_j \exp[-(\mathbf{x} - \mathbf{x_j})^2/d^2]$), where the size d is set as 12.5 km and the location $\mathbf{x_j}$ is shown in Fig. 15b. We estimated coefficient a_j with a damped-least-square inversion analysis by using the sea-surface height change at the hypothetical observation points (Inazu and Saito, 2014). The locations of the hypothesized stations and the elements of the sea-surface height are the same as those used in Inazu et al. (2016).

For example, Fig. 16a shows the estimated initial height tsunami distribution $u_z^e(x,y)$ where we used the sea-surface waveforms for 3 min from the start of the earthquake. The estimated initial height distribution was small compared to the hypothesized sea-surface height distribution in the simulation. In order to quantify a size for the tsunami source, we introduced a volume V_0 defined as,

$$V_0 = \iint_{u_z^e \geq u_0} u_z^e(x,y)dS. \tag{11}$$

The integration was conducted over the area where the initial tsunami height was higher than 0.1 m (u_0 = 0.1 m). The volume V_0 was estimated at 14 km^3 for the estimated initial height distribution (Fig. 16a). The volume was V_0 = 24 km^3 for the original initial height distribution (Fig. 15c).

We then calculated the tsunami inundation into the city from the estimated initial height distribution $u_z^e(x,y)$ but did not include the topography/bathymetry change caused by the permanent displacement

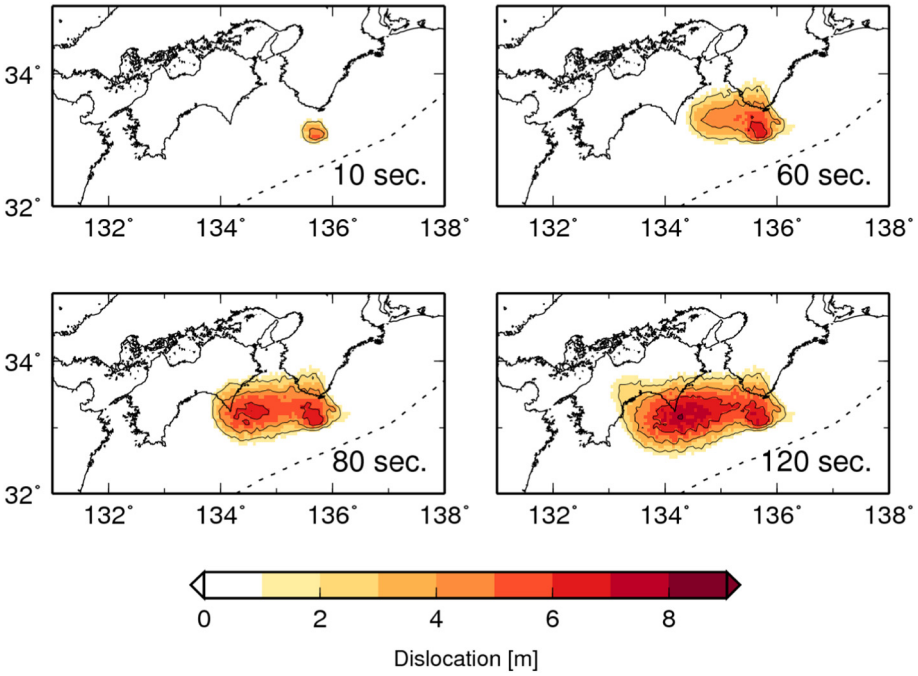

Fig. 9. An earthquake rupture scenario constructed by Hok et al. (2011). Temporal change in the dislocation distribution along the plate boundary is plotted.

due to the earthquake (Fig. 16b). Since the estimated initial tsunami height distribution (V_0 = 14 km^3) was underestimated compared to the original initial height distribution (V_0 = 24 km^3), the predicted inundation area was smaller than the inundation area simulated in Fig. 14b. If we include the permanent displacement, the estimated sea-surface height reasonably predicted the inundation area (Fig. 16c).

Fig. 17a shows the estimated initial tsunami height distribution when we used the sea-surface waveforms for 20 min from the earthquake rupture start. Fig. 18a shows the estimated height distribution, which closely reproduced the originally hypothesized sea-surface height distribution. The volume V_0 (Eq. (11)) for the estimated initial height distribution was estimated to be 22 km^3 in this case. This is almost the same as the value of the originally hypothesized sea-surface height distribution of 24 km^3. We calculated the inundation area without considering the topography change (Fig. 17b). This roughly reproduced the inundation area, although this still underestimated the inundation by the hypothesized earthquake scenario in some places. Fig. 17c shows the result of the inundation when the topography change caused by the permanent displacement is included. Fig. 17c reproduced the hypothesized inundation area better than Fig. 17b by introducing the subsidence of the city area in the inundation calculation.

Table 1
The layered structure used in the simulation.

Depth [km]	V_S [km/s]	V_P [km/s]	ρ [10^3 kg/m^3]
Water layer	0.0	1.45	1.02
–16	3.2	5.8	2.6
16–25.4	3.9	6.8	2.9
25.4–	4.49	8.1	3.3

Fig. 18 shows the estimated initial height distribution volume V_0 with expanded observation time. This indicates that we could estimate the volume of the initial tsunami height distribution more precisely if we use a longer observation period. We estimated the initial tsunami volume with some accuracy if the analyzed record length is longer than 10 min for this case (the rupture duration of this event was ~150 s). We should note that the inundation area in Kochi city was more precisely estimated when we used an inaccurate initial height distribution including the topography change (Fig. 16c) than when we used a better initial height distribution without including the topography change (Fig. 17b). This indicates the importance of the permanent displacement at the coasts for the tsunami inundation.

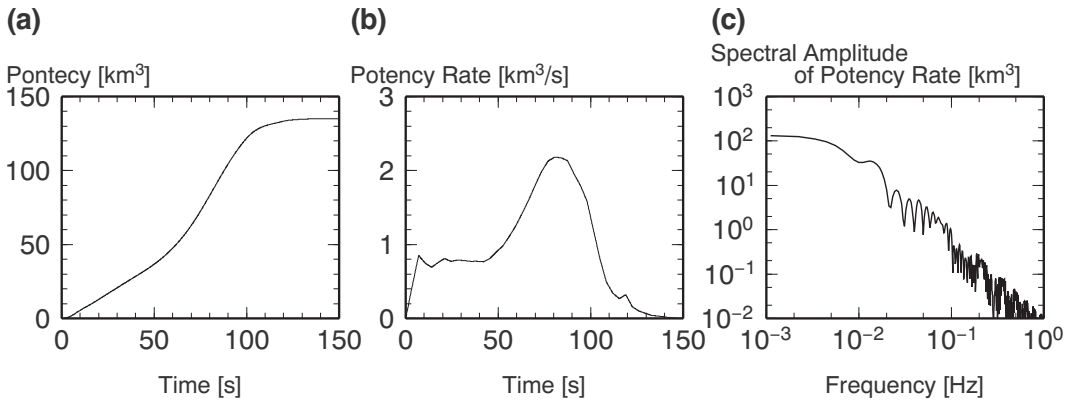

Fig. 10. (a) Temporal change in the potency, (b) the potency rate, and (c) the spectral amplitude of the potency rate.

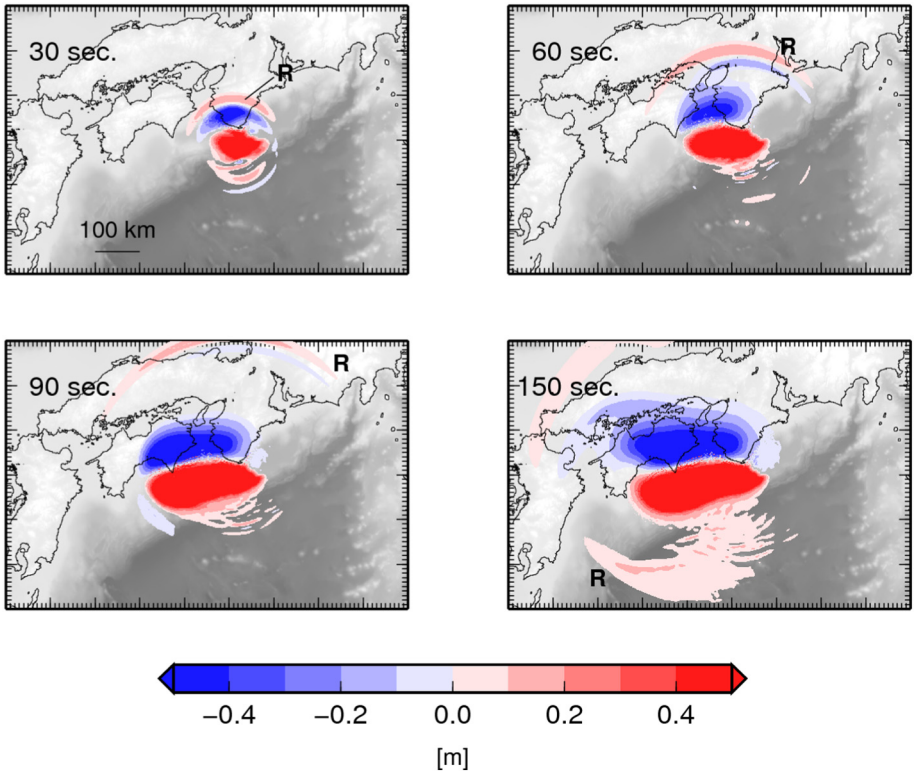

Fig. 11. Vertical displacements at elapsed times of 30, 60, 90 and 150 s derived from the 3-D seismic wave simulation using the rupture model shown in Fig. 10. Rayleigh wave is marked by R.

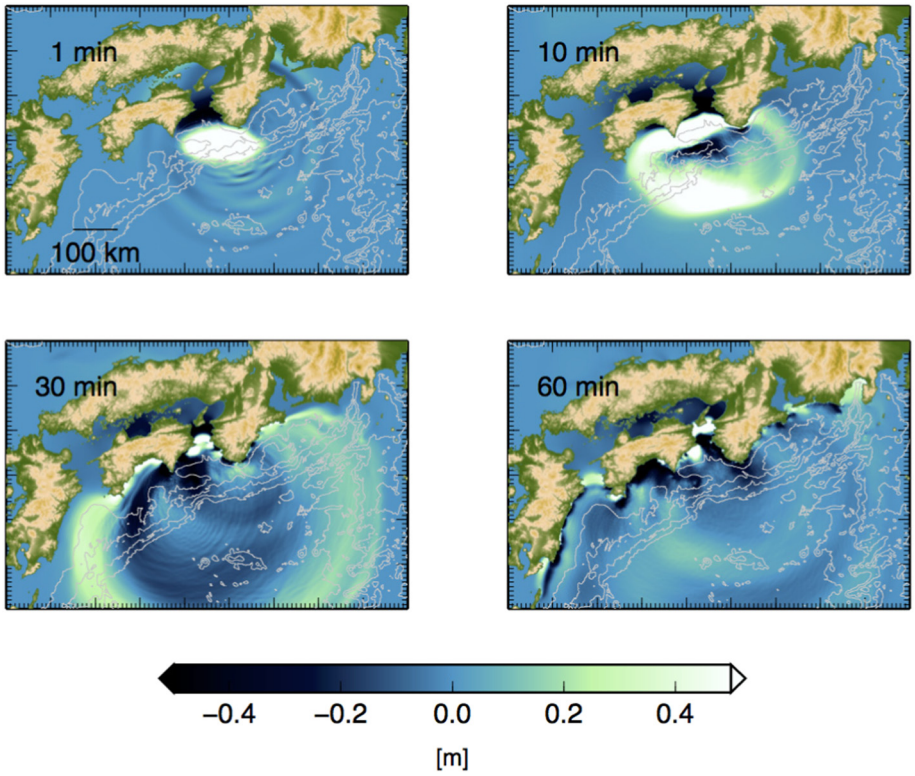

Fig. 12. Vertical displacement of the sea surface at elapsed times of 1, 10, 30 and 60 min derived from the 2-D nonlinear long-wave tsunami simulation using the results of seismic-wave simulation as a source.

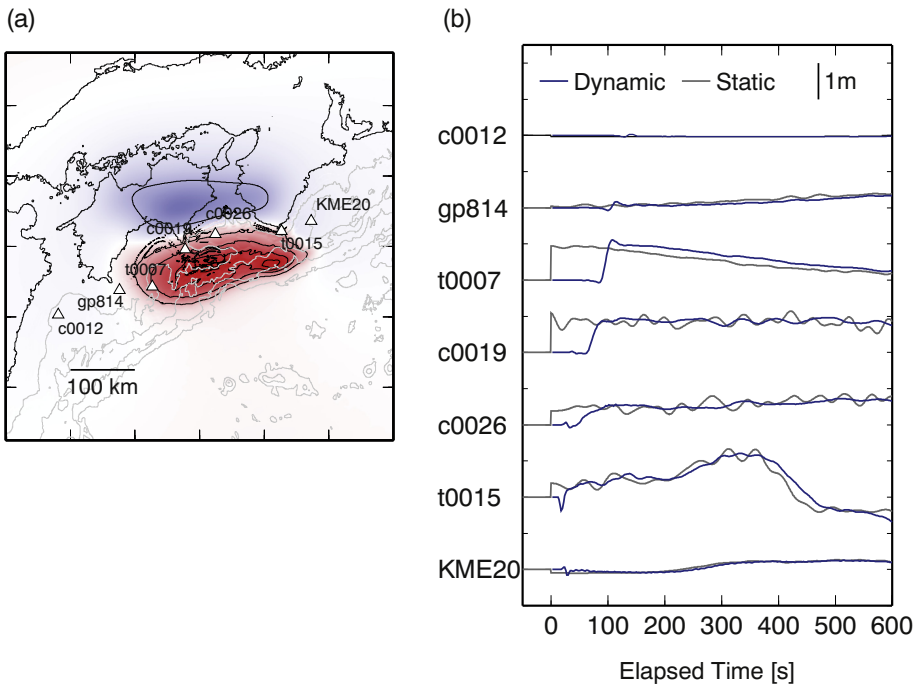

Fig. 13. (a) Hypothetical station locations and the permanent sea-surface displacement calculated by the seismic simulation. (b) Waveforms of vertical displacement on the sea surface at the hypothetical stations. The waveforms synthesized by using the time and spatial varying sea-surface displacements as source are plotted by blue lines. The waveforms synthesized by using the time-invariant initial tsunami height distribution are plotted by black lines. The low-pass filter (> 60 s) is applied to all the waveforms. (For interpretation of the references to color in this figure legend, the reader is referred to the web version of this article.)

5. Discussion

5.1. Waveform synthesis including seismic waves and tsunami

This study synthesized the sea surface height change by including seismic waves and tsunami. Some past studies proposed methods including seawater compressibility but did not include solid earth elasticity to synthesize sea surface height change (e.g., Yamamoto, 1982; Stiassnie, 2010; Sammarco et al., 2013). The wave is often referred to as an acoustic gravity wave. These studies usually assumed that the sea bottom was rigid. On the other hand, the sediment on the ocean bottom is sometimes far from rigid. Nosov and Kolesov (2007) analyzed the observed ocean acoustic waves by assuming soft sediments at the sea bottom. Takemura et al. (2018) demonstrated that a low-velocity layer along the Nankai trough strongly affects the seismic surface waves. The method proposed in this study can synthesize waveforms while including the subsurface elastic inhomogeneity.

Contrary to the studies on acoustic gravity waves (e.g., Yamamoto, 1982; Stiassnie, 2010; Sammarco et al., 2013), the method in this study includes the effect of the compressibility only for seismic waves but not for tsunami. The seawater compressibility makes the tsunami propagation velocity slightly smaller (e.g., Nakamura, 1961; Yamamoto, 1982; Watada et al., 2014). The combination of recently developed observations and well-estimated tsunami source models can detect such fractional velocity reduction when tsunamis propagate over long distances (> ~7000 km) (e.g., Inazu and Saito, 2013; Tsai et al., 2013; Watada et al., 2014). However, note that this effect is negligible for tsunami propagation over short distances (< ~1000 km).

Normal mode theory, including an appropriate dynamic boundary condition at the sea surface, can reproduce tsunami in addition to seismic waves (e.g., Ward, 1980; Okal, 1982; Comer, 1984; Panza et al., 2000). Recent studies conducted numerical simulations to reproduce both seismic waves and tsunami. Some studies were conducted in 2-D space (e.g., Eyov et al., 2013; Lotto and Dunham, 2015; Lotto et al., 2017). Maeda et al. (2013) conducted 3-D simulations for seismic waves and tsunami. If we employ an equal increment of time for seismic wave propagation and tsunami propagation, it will require too much computation time, because the time scale of tsunami is much longer than that of seismic waves. To reduce the computational costs, after the seismic waves have left the region of interest, we should pass the sea surface height and depth-averaged horizontal particle velocity to a more efficient tsunami simulation code for calculating inundation and longer time tsunami propagation. The method proposed in this paper is an alternative way of simulating both seismic waves and tsunami by the two-step method.

5.2. Sea-surface height change and sea-bottom pressure change

This study investigated the records of sea surface height change, while sea bottom pressure records have become more widely used at present (e.g., An et al., 2017; Kubota et al., 2017, 2018a, 2018b). We discuss both the difference in seismic waves on sea surface height change and on sea bottom pressure change.

The pressure change at the sea-bottom is given by

$$p_e = p_{gravity} - \sigma \tag{12}$$

where $p_{gravity}$ is the pressure change originating from gravity and σ is stress change caused by seismic motion but independent of gravity. Three-dimensional water wave theory gives the pressure change at the sea bottom $p_{gravity}$ caused by the sea-surface height distribution $\eta(x,y,t)$ as

$$\mathrm{p_{gravity}} = \rho_0 g_0 \frac{1}{(2\pi)^2} \int_{-\infty}^{\infty} \int_{-\infty}^{\infty} \frac{\hat{\eta}(\mathrm{k_x}, \mathrm{k_y}, \mathrm{t})}{\cosh(\mathrm{kh_0})} \mathrm{e}^{\mathrm{i(k_x x + k_y y)}} \mathrm{dk_x dk_y}$$

for a constant sea depth of h_0 where ρ_0 is the seawater density, $\hat{\eta}(k_x, k_y, t)$ is the 2-D spatial Fourier transform of $\eta(x,y,t)$ and $k = \sqrt{k_x^2 + k_y^2}$ (e.g., Saito, 2010; Saito, 2019). Additionally, if we include the static pressure change caused by the vertical displacement u_{bottom} at the sensor location, the pressure change is given by

$$p_{gravity} = \rho_0 g_0 \left[\frac{1}{(2\pi)^2} \int_{-\infty}^{\infty} \int_{-\infty}^{\infty} \frac{\hat{\eta}(k_x, k_y, t)}{cosh(kh_0)} e^{i(k_x x + k_y y)} dk_x dk_y - u_{bottom} \right]. \tag{13}$$

When the period of the seismic motion is longer than $T > 4h_0/c_0$ (~10 s when h_0 = 4 km and c_0 = 1.6 km/s), the ocean acoustic waves does not exist (in other words, *P*-waves cannot be trapped within the sea layer) (e.g., Nosov and Kolesov, 2007; Saito, 2019). In that case, the stress change σ caused by seismic motion is given by incompressible

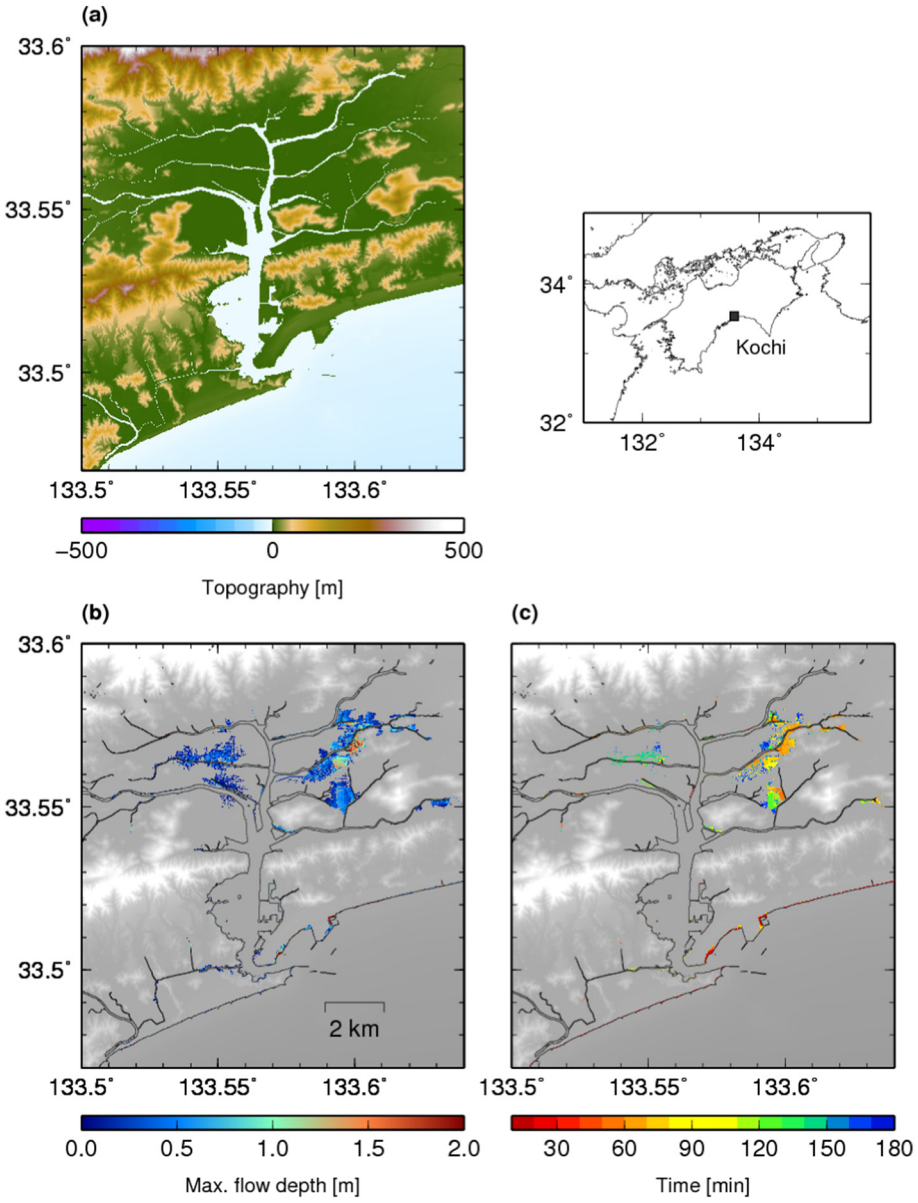

Fig. 14. (a) Topography in Kochi city. (b) Flow depth distribution. (c) The distribution of the time when the flow depth exceeds 0.3 m.

fluid dynamics as

$$\sigma = -\frac{\rho_0 h_0}{(2\pi)^2}\int_{-\infty}^{\infty}\int_{-\infty}^{\infty}\frac{tanh(kh_0)}{kh_0}\hat{a}_z^{bottom}(k_x,k_y,t)e^{i(k_x x+k_y y)}dk_x dk_y \tag{14}$$

where $\hat{a}_z^{bottom}(k_x,k_y,t)$ is the 2-D spatial Fourier transform of the vertical acceleration at the sea bottom $a_z(x,y,t)=\ddot{u}_{bottom}(x,y,t)$ (Saito, 2013; Saito, 2017). Eq. (12) with Eqs. (13) and (14) gives the pressure change caused by tsunami and seismic motion for periods longer than $T > 4h_0/c_0$.

For simplicity, we assume that the wavelength is much longer than the sea depth $kh_0 \ll 1$. Then, Eq. (13) is approximated by $p_{static} \sim \rho_0 g_0(\eta - u_{bottom})$ and Eq. (14) is approximated by $\sigma \sim -\rho_0 h_0 \ddot{u}_{bottom}$ (e.g., Filloux, 1982; Webb, 1998; Matsumoto et al., 2012; Saito and Tsushima, 2016). Then, Eq. (12) becomes

$$p_e \approx \rho_0 g_0(\eta - u_{bottom}) + \rho_0 h\ddot{u}_{bottom} \text{ for } kh_0 \ll 1. \tag{15}$$

Eq. (15) represents the sea-bottom pressure change for $T > 4h_0/c_0$ and $kh_0 \ll 1$.

A red line in Fig. 19a shows the ocean-bottom pressure records synthesized based on Eq. (15). The low-pass filter with the cut-off period of 60 s was applied to the records, which removes the ocean acoustic waves. The pressure records without seismic waves is given by $p_e = \rho g(\eta - u_{\mathrm{bottom}})$ (a gray line in Fig. 19a). The comparison clearly indicates that the pressure change caused by the seismic waves appears as a pulse at the elapsed time of ~100 s, reaching ~0.5 m H_2O at the maximum. Since this pulse is not a tsunami but a seismic wave, this can be regarded as noise for tsunami signal analysis.

Fig. 19b shows the surface height record at the same point. The surface height records including and excluding seismic waves are plotted with red and black lines respectively. We synthesized the surface height records excluding seismic waves by using the permanent sea-surface displacement as the initial tsunami height distribution. Unlike the case of the pressure records, there are no large differences between the records including seismic waves (red line) and those excluding seismic waves (gray line). This indicates that the effect of seismic waves on tsunami records is less important in sea-surface height records than sea-bottom pressure records. The difference comes from the contrasting mechanism of the seismic-wave contribution to records from the displacement and pressure change. With regards to

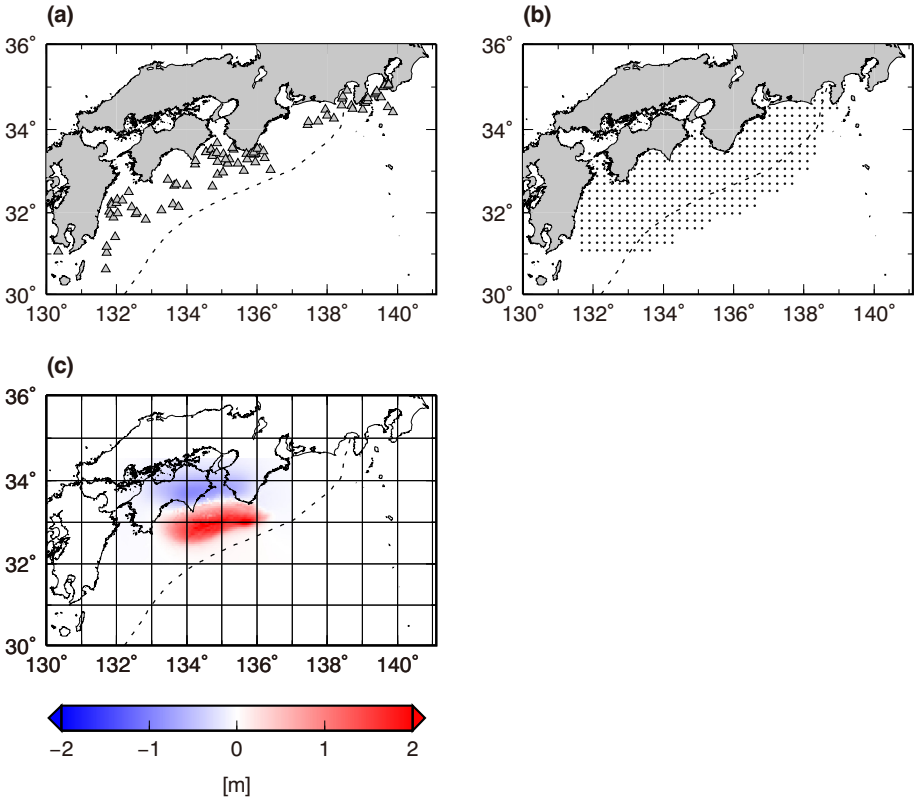

Fig. 15. (a) Hypothetical observation points used in a numerical experiment. Each observation point records sea-surface height change. (b) The locations of sea-surface height elements. (c) The sea-surface height distribution at the elapsed time of 600 s calculated by the seismic wave simulation as permanent displacement.

displacement at the sea surface, seismic waves work in addition to the surface displacement $d = \eta + u_{surface}$ where d is sea-surface height records, η is tsunami height, and $u_{surface}$ is vertical displacement caused by seismic waves. However, for the pressure change at the sea-bottom, the stress change σ caused by the seismic wave contributes to the ocean-bottom pressure records as $p_{gravity} - \sigma$ where $p_{gravity}$ is the pressure change originating from gravity and σ is the stress change caused by seismic motion. The stress change σ is approximately given by $\sigma \sim -\rho_0 h\ddot{u}_{\mathrm{bottom}}$ when the frequency is low $\omega \ll c_0/h$ where c_0 is the phase velocity of ocean acoustic waves. The relation $\sigma \sim -\rho h\ddot{u}_{\mathrm{bottom}}$ is theoretically derived for a constant sea depth and it is also confirmed empirically in real observations (e.g., Filloux, 1982; Webb, 1998; Matsumoto et al., 2012; Saito and Tsushima, 2016; Saito, 2019). The pressure change is proportional to the acceleration rather than displacement.

We should note that we cannot decompose seismic waves and tsunami in an observed waveform record, where the waveform is recorded by either change in ocean-bottom pressure or the sea-surface displacement. However, if we can use both the sea-bottom pressure change record and the sea-surface displacement record, by effectively using the

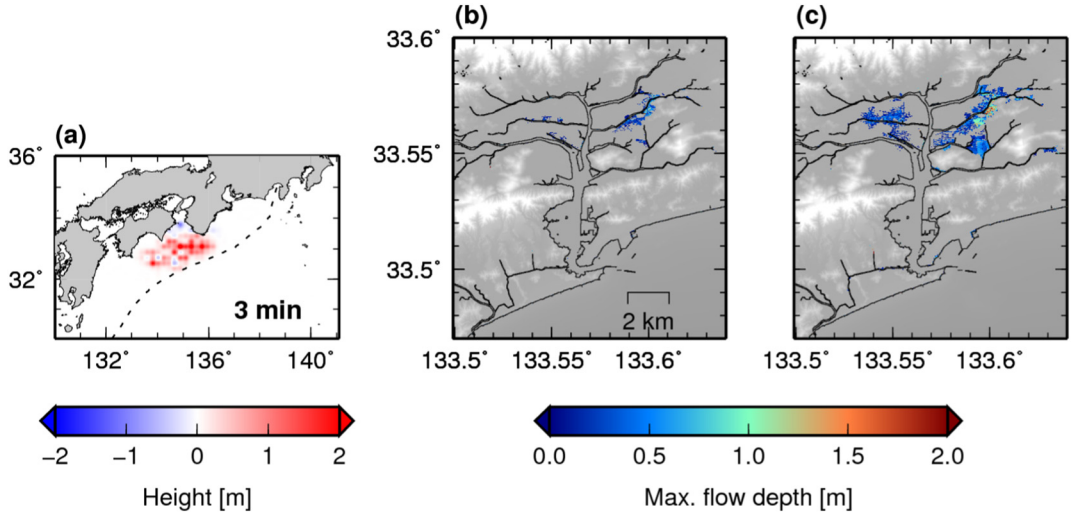

Fig. 16. (a) The estimated initial tsunami height distribution when the surface height change from 0 min to 3 min is used. (b) The inundation area in the city calculated from the estimated tsunami height distribution where the permanent displacement is not included. (c) The inundation area from the estimated tsunami height distribution where the permanent displacement is included.

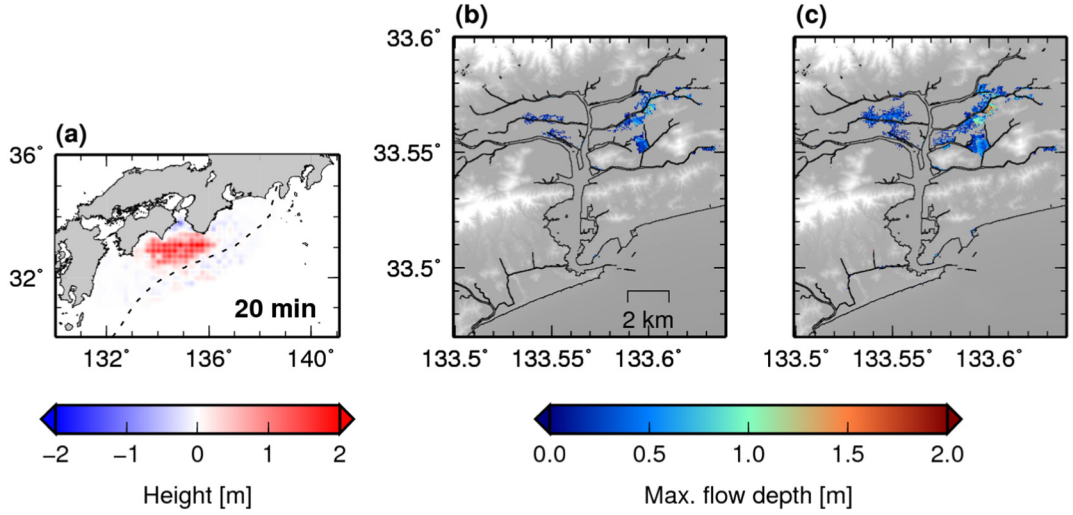

Fig. 17. (a) The estimated initial tsunami height distribution when the surface height change from 0 min to 20 min is used. (b) The inundation area in the city calculated from the estimated tsunami height distribution where the permanent displacement is not included. (c) The inundation area from the estimated tsunami height distribution where the permanent displacement is included.

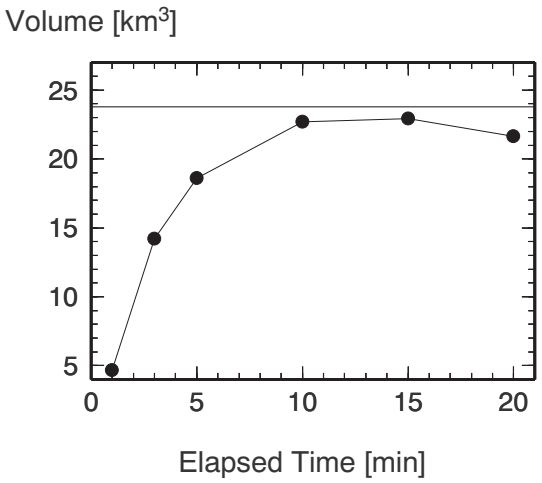

Fig. 18. The volume defied by Eq. (11) as a function of the elapsed time.

two different excitation mechanisms of seismic waves, it would be possible to decompose the tsunami signal from the seismic signal. Also, if ocean-bottom seismometers are installed near the pressure gauges, it would be useful to analyze the seismograms to decompose tsunami and seismic signals in the pressure records. At present, sea-surface height observation is not widely conducted compared to the sea-bottom pressure change observation. An integrated analysis of pressure record and the displacement at the sea surface and sea bottom may give another possibility of precise tsunami observation inside the focal area. Recently, Tsushima et al. (2012) proposed an inversion method to decompose the permanent sea-bottom uplift and the tsunami signals using only ocean bottom pressure records. They reported that it would take about 5 min to obtain a stable solution. However, if different kinds of data such as displacements and pressure change are available, we might obtain a reliable solution in shorter elapsed time. Therefore, the development of the sea-surface height observation and displacement observation inside the focal area would promise advances in tsunami research.

6. Conclusions

This study showed an efficient method of calculating sea-surface height change, including the contributions from both seismic waves and tsunami, although most past studies have usually neglected the contribution of seismic waves. We synthesized the sea surface height records for an anticipated earthquake rupture scenario that could possibly occur in the Nankai Trough, Japan. By using this hypothetical data set, we can evaluate the performance of the real-time tsunami prediction

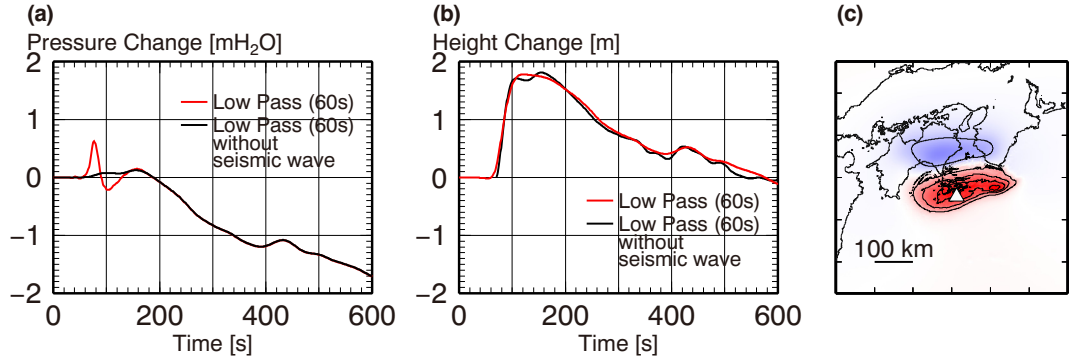

Fig. 19. (a) Pressure change on the sea bottom at a station inside the focal area. Comparisons between the synthesized waveform considering seismic wave (red lines) and without considering seismic wave (gray lines). (b) Sea surface height change at the station 06. The low-pass filter (> 60 s) is applied to all the waveforms. (c) The location of the hypothesized sensor used in (a) and (b). (For interpretation of the references to color in this figure legend, the reader is referred to the web version of this article.)

method using sea surface height records. We reliably estimated the source size when we used the sea-surface height records for ~10 min from the start of an earthquake rupture and we assumed a rupture scenario similar to the 1946 Nankai earthquake. We should note that seismic waves appear in both surface-height records and ocean-bottom pressure records. A numerical result showed that the seismic-wave contribution was smaller in the sea surface height record than the sea bottom pressure record. It would be useful to develop precise and reliable sea surface height measurement and use both sea-bottom pressure records and sea-surface height records for rapid data analysis inside the focal area.

Authors' contributions

TS, TB, and DI drafted this manuscript. All authors approved the manuscript.

TS developed a synthesis method. TB performed the numerical simulations of the tsunami propagation and inundation. DI performed the tsunami inversion analysis. ST performed the numerical simulations of the seismic wave propagation. EF prepared the earthquake fault rupture model. All authors equally contributed to scientific discussions. All authors read and approved the final manuscript.

Acknowledgements

E. Duham reviewed this manuscript and gave important comments and suggestions. T. Maeda gave important comments and suggestions. Hypothesized station locations in numerical experiments are obtained from Inazu et al. (2016). This work was supported by JSPS KAKENHI Grant Number 19K04021.

References

Aki, K., Richards, P.G., 2002. Quantitative Seismology. University Science Books.
Amante, C., Eakins, B.W., 2009. ETOPO1 1 Arc-minute Global Relief Model: Procedures, Data Sources and Analysis. NOAA Technical Memorandum NESDIS NGDC-24. National Geophysical Data Center, NOAAhttps://doi.org/10.7289/V5C8276M.
An, C., Cai, C., Zheng, Y., Meng, L., Liu, P., 2017. Theoretical solution and applications of ocean bottom pressure induced by seismic seafloor motion. Geophys. Res. Lett. 44 (20). https://doi.org/10.1002/2017GL075137.
Baba, T., et al., 2016. Large-scale, high-speed tsunami prediction for the Great Nankai Trough Earthquake on the K computer. Int. J. High Perform. Comput. Appl. 30 (1), 71–84. https://doi.org/10.1177/1094342015584090.
Baba, T., et al., 2017. Accurate numerical simulation of the far-field tsunami caused by the 2011 Tohoku earthquake, including the effects of Boussinesq dispersion, seawater density stratification, elastic loading, and gravitational potential change. Ocean Model 111, 46–54. https://doi.org/10.1016/j.ocemod.2017.01.002.
Comer, R.P., 1984. Tsunami generation: a comparison of traditional and normal mode approaches. Geophys. J. Int. 77 (1), 29–41.
Dettmer, J., Hawkins, R., Cummins, P.R., Hossen, J., Sambridge, M., Hino, R., Inazu, D., 2016. Tsunami source uncertainty estimation: the 2011 Japan tsunami. J. Geophys. Res. Solid Earth 121, 4483–4505. https://doi.org/10.1002/2015JB012764.
Dziewonski, A.M., Anderson, D.L., 1981. Preliminary reference Earth model. Phys. Earth Planet. Inter. 25 (4), 297–356. https://doi.org/10.1016/0031-9201(81)90046-7.
Eyov, E., Klar, A., Kadri, U., Stiassnie, M., 2013. Progressive waves in a compressible-ocean with an elastic bottom. Wave Motion 50 (5), 929–939. https://doi.org/10.1016/j.wavemoti.2013.03.003.
Filloux, J., 1982. Tsunami recorded on the open ocean floor. Geophys. Res. Lett. 9 (1), 25–28.
Foster, J.H., Brooks, B.A., Wang, D., Carter, G.S., Merrifield, M.A., 2012. Improving tsunami warning using commercial ships. Geophys. Res. Lett. 39, L09603. https://doi.org/10.1029/2012GL051367.
Furumura, T., Saito, T., 2009. Integrated ground motion and tsunami simulation for the 1944 Tonankai earthquake using high-performance supercomputers. J. Disaster Res. 4, 118–126.
Furumura, T., Imai, K., Maeda, T., 2011. A revised tsunami source model for the 1707 Hoei earthquake and simulation of tsunami inundation of Ryujin Lake, Kyushu, Japan. J. Geophys. Res. 116, B02308. https://doi.org/10.1029/2010JB007918.
González, F.I., Kulikov, Y.A., 1993. Tsunami dispersion observed in the deep ocean. In: Tinti, S. (Ed.), Tsunamis in the World. Kluwer Acad, Dordrecht, Netherlands, pp. 7–16.
Graves, R.W., 1996. Simulating seismic wave propagation in 3D elastic media using staggered-grid finite differences. Bull. Seismol. Soc. Am. 86 (4), 1091–1106.
Gusman, A.R., Seehan, A.F., Satake, K., Heidarzadeh, M., Mulia, I.E., Maeda, T., 2016. Tsunami data assimilation of Cascadia seafloor pressure gauge records from the 2012 Haida Gwaii earthquake. Geophys. Res. Lett. 43, 4189–4196. https://doi.org/10.1002/2016GL068368.
Hayashi, Y., 2010. Empirical relationship of tsunami height between offshore and coastal stations. Earth Planets Space 62 (3), 269–275. https://doi.org/10.5047/eps.2009.11.006.
Heidarzadeh, M., Murotani, S., Satake, K., Takagawa, T., Saito, T., 2017. Fault size and depth extent of the Ecuador earthquake (Mw 7.8) of 16 April 2016 from teleseismic and tsunami data. Geophys. Res. Lett. 44 (5), 2211–2219. https://doi.org/10.1002/2017GL072545.
Hok, S., Fukuyama, E., Hashimoto, C., 2011. Dynamic rupture scenarios of anticipated Nankai-Tonankai earthquakes, southwest Japan. J. Geophys. Res. Solid Earth 116 (B12). https://doi.org/10.1029/2011JB008492.
Inazu, D., Saito, T., 2013. Simulation of distant tsunami propagation with a radial loading deformation effect. Earth Planets Space 65 (8), 835–842. https://doi.org/10.5047/eps.2013.03.010.
Inazu, D., Saito, T., 2014. Two subevents across the Japan Trench during the 7 December 2012 off Tohoku earthquake (Mw 7.3) inferred from offshore tsunami records. J. Geophys. Res. Solid Earth 119 (7), 5800–5813. https://doi.org/10.1002/2013JB010892.
Inazu, D., Waseda, T., Hibiya, T., Ohta, Y., 2016. Assessment of GNSS-based height data of multiple ships for measuring and forecasting great tsunamis. Geosci. Lett. 3 (1), 25. https://doi.org/10.1186/s40562-016-0059-y.
Ishibashi, K., 2004. Status of historical seismology in Japan. Ann. Geofis. 47 (2–3), 339–368. https://doi.org/10.4401/ag-3305.
Kajiura, K., 1963. The leading wave of a tsunami. Bull. Earthequake Res. Inst. 41, 535–571.
Kato, T., Terada, Y., Kinoshita, M., Kakimoto, H., Isshiki, H., Matsuishi, M., Yokoyama, A., Tanno, T., 2000. Real-time observation of tsunami by RTK-GPS. Earth Planets Space 52 (10), 841–845. https://doi.org/10.1186/bf03352292.
Kervella, Y., Dutykh, D., Dias, F., 2007. Comparison between three-dimensional linear and nonlinear tsunami generation models. Theor. Comput. Fluid Dyn. 21 (4), 245–269. https://doi.org/10.1007/s00162-007-0047-0.
Kim, S., Saito, T., Fukuyama, E., Kang, T.S., 2016. The Nankai Trough earthquake tsunamis in Korea: numerical studies of the 1707 Hoei earthquake and physics-based scenarios. Earth Planets Space 68. https://doi.org/10.1186/s40623-016-0438-9.
Kirby, J.T., Shi, F.Y., Tehranirad, B., Harris, J.C., Grilli, S.T., 2013. Dispersive tsunami waves in the ocean: model equations and sensitivity to dispersion and Coriolis effects. Ocean Model 62, 39–55. https://doi.org/10.1016/j.ocemod.2012.11.009.
Kubota, T., Saito, T., Suzuki, W., Hino, R., 2017. Estimation of seismic centroid moment tensor using ocean bottom pressure gauges as seismometers. Geophys. Res. Lett. 44 (21), 10, 907–10,915. https://doi.org/10.1002/2017GL075386.
Kubota, T., et al., 2018a. Using tsunami waves reflected at the coast to improve offshore earthquake source parameters: application to the 2016 Mw 7.1 Te Araroa earthquake, New Zealand. J. Geophys. Res. Solid Earth 123 (10), 8767–8779. https://doi.org/10.1029/2018JB015832.
Kubota, T., Suzuki, W., Nakamura, T., Chikasada, N.Y., Aoi, S., Takahashi, N., Hino, R., 2018b. Tsunami source inversion using time-derivative waveform of offshore pressure records to reduce effects of non-tsunami components. Geophys. J. Int. 215 (2), 1200–1214. https://doi.org/10.1093/gji/ggy345.
Kumagai, H., 1996. Time sequence and the recurrence models for large earthquakes along the Nankai trough revisited. Geophys. Res. Lett. 23 (10), 1139–1142. https://doi.org/10.1029/96GL01037.
Lotto, G.C., Dunham, E.M., 2015. High-order finite difference modeling of tsunami generation in a compressible ocean from offshore earthquakes. Comput. Geosci. 19, 327. https://doi.org/10.1007/s10596-015-9472-0.
Lotto, G.C., Dunham, E.M., Jeppson, T.N., Tobin, H.J., 2017. The effect of compliant prisms on subduction zone earthquakes and tsunamis. Earth Planet. Sci. Lett. 458, 213–222. https://doi.org/10.1016/j.epsl.2016.10.050.
Maeda, T., Furumura, T., 2013. FDM simulation of seismic waves, ocean acoustic waves, and tsunamis based on tsunami-coupled equations of motion. Pure Appl. Geophys. 170 (1–2), 109–127. https://doi.org/10.1007/s00024-011-0430-z.
Maeda, T., Furumura, T., Noguchi, S., Takemura, S., Sakai, S., Shinohara, M., Iwai, K., Lee, S.J., 2013. Seismic and tsunami wave propagation of the 2011 off the Pacific Coast of Tohoku Earthquake as inferred from the tsunami-coupled finite difference simulation. Bull. Seismol. Soc. Am. 103 (2B), 1456–1472. https://doi.org/10.1785/0120120118.
Maeda, T., Obara, K., Shinohara, M., Kanazawa, T., Uehira, K., 2015. Successive estimation of a tsunami wavefield without earthquake source data: a data assimilation approach toward real-time tsunami forecasting. Geophys. Res. Lett. 42 (19), 7923–7932. https://doi.org/10.1002/2015gl065588.
Matsumoto, H., Inoue, S., Ohmachi, T., 2012. Dynamic response of bottom water pressure due to the 2011 Tohoku earthquake. J. Disaster Res. 7 (sp), 468–475. https://doi.org/10.20965/jdr.2012.p0468.
Miyoshi, T., Saito, T., Inazu, D., Tanaka, S., 2015. Tsunami modeling from the seismic CMT solution considering the dispersive effect: a case of the 2013 Santa Cruz Islands tsunami. Earth Planets Space 67 (1), 4. https://doi.org/10.1186/s40623-014-0179-6.
Mulia, I.E., Inazu, D., Waseda, T., Gusman, A.R., 2017. Preparing for the future Nankai Trough tsunami: a data assimilation and inversion analysis from various observational systems. J. Geophys. Res. Oceans 122, 7924–7937. https://doi.org/10.1002/2017JC012695.
Nakamura, K., 1961. Velocity of long gravity waves in the ocean, geophysics, Ser. 5. In: Tohoku University Science Reports.
Nakamura, T., Takenaka, H., Okamoto, T., Kaneda, Y., 2012. FDM simulation of seismic-wave propagation for an aftershock of the 2009 Suruga Bay earthquake: effects of ocean-bottom topography and Seawater Layer. Bull. Seismol. Soc. Am. 102 (6), 2420–2435. https://doi.org/10.1785/0120110356.

Namegaya, Y., Tanioka, Y., Abe, K., Satake, K., Hirata, K., Okada, M., Gusman, A.R., 2009. In situ measurements of tide gauge response and corrections of tsunami waveforms from the Niigataken Chuetsu-oki Earthquake in 2007. Pure Appl. Geophys. 166 (1–2), 97–116. https://doi.org/10.1007/s00024-008-0441-6.

Nosov, M.A., Kolesov, S.V., 2007. Elastic oscillations of water column in the 2003 Tokachi-oki tsunami source: in-situ measurements and 3-D numerical modeling. Nat. Hazards Earth Syst. Sci. 7 (2), 243–249.

Ohminato, T., Chouet, B.A., 1997. A free-surface boundary condition for including 3D topography in the finite-difference method. Bull. Seismol. Soc. Am. 87 (2), 494–515.

Okada, Y., 1985. Surface deformation due to shear and tensile faults in a half-space. Bull. Seismol. Soc. Am. 75 (4), 1135–1154.

Okal, E.A., 1982. Mode-wave equivalence and other asymptotic problems in tsunami theory. Phys. Earth Planet. Inter. 30, 1–11.

Panza, G.F., Romanelli, F., Yanovskaya, T.B., 2000. Synthetic tsunami mareograms for realistic oceanic models. Geophys. J. Int. 141 (2), 498–508. https://doi.org/10.1046/j.1365-246x.2000.00100.x.

Saito, T., 2010. Love-wave excitation due to the interaction between a propagating ocean wave and the sea-bottom topography. Geophys. J. Int. https://doi.org/10.1111/j.1365-246X.2010.04695.x.

Saito, T., 2013. Dynamic tsunami generation due to sea-bottom deformation: analytical representation based on linear potential theory. Earth Planets Space 65 (12), 1411–1423. https://doi.org/10.5047/eps.2013.07.004.

Saito, T., 2017. Tsunami generation: validity and limitations of conventional theories. Geophys. J. Int. 210 (3), 1888–1900. https://doi.org/10.1093/gji/ggx275.

Saito, T., 2019. Tsunami Generation and Propagation. Springer.

Saito, T., Tsushima, H., 2016. Synthesizing ocean bottom pressure records including seismic wave and tsunami contributions: toward realistic tests of monitoring systems. J. Geophys. Res. Solid Earth 121, 8175–8195. https://doi.org/10.1002/2016JB013195.

Saito, T., Satake, K., Furumura, T., 2010a. Tsunami waveform inversion including dispersive waves: the 2004 earthquake off Kii Peninsula, Japan. J. Geophys. Res. Solid Earth 115. https://doi.org/10.1029/2009jb006884.

Saito, T., Matsuzawa, T., Obara, K., Baba, T., 2010b. Dispersive tsunami of the 2010 Chile earthquake recorded by the high-sampling-rate ocean-bottom pressure gauges. Geophys. Res. Lett. 37. https://doi.org/10.1029/2010gl045290.

Sammarco, P., Cecioni, C., Bellotti, G., Abdolali, A., 2013. Depth-integrated equation for large-scale modelling of low-frequency hydroacoustic waves. J. Fluid Mech. 722, R6. https://doi.org/10.1017/jfm.2013.153.

Satake, K., 2015. Tsunamis. In: Treatise on Geophysics, Second edition. pp. 477–504.

Seno, T., Stein, S., Gripp, A.E., 1993. A model for the motion of the Philippine Sea Plate consistent with NUVEL-1 and geological data. J. Geophys. Res. Solid Earth 98 (B10), 17941–17948. https://doi.org/10.1029/93jb00782.

Stiassnie, M., 2010. Tsunamis and acoustic-gravity waves from underwater earthquakes. J. Eng. Math. 67 (1–2), 23–32.

Takahashi, R., 1942. On the seismic sea waves caused by deformation of the sea bottom. Bull. Earthq. Res. Inst., Univ. Tokyo 20, 357–400.

Takemura, S., Furumura, T., Maeda, T., 2015. Scattering of high-frequency seismic waves caused by irregular surface topography and small-scale velocity inhomogeneity. Geophys. J. Int. 201 (1), 459–474. https://doi.org/10.1093/gji/ggv038.

Takemura, S., et al., 2018. Modeling of long-period ground motions in the Nankai subduction zone: model simulation using the accretionary prism derived from oceanfloor local S-wave velocity structures. Pure Appl. Geophys. https://doi.org/10.1007/s00024-018-2013-8.

Tang, L., Titov, V.V., Chamberlin, C.D., 2009. Development, testing, and applications of site-specific tsunami inundation models for real-time forecasting. J. Geophys. Res. Oceans 114. https://doi.org/10.1029/2009jc005476.

Tanioka, Y., 2000. Numerical simulation of far-field tsunamis using the linear Boussinesq equation - the 1998 Papua New Guinea tsunami. Pap. Meteorol. Geophys. 51, 17–25. https://doi.org/10.2467/mripapers.51.17.

Titov, V.V., Gonzalez, F.I., Bernard, E., Eble, M.C., Mofjeld, H.O., Newman, J.C., Venturato, A.J., 2005. Real-time tsunami forecasting: challenges and solutions. Nat. Hazards 35 (1), 35–41. https://doi.org/10.1007/s11069-004-2403-3.

Tsai, V.C., Ampuero, J.P., Kanamori, H., Stevenson, D.J., 2013. Estimating the effect of Earth elasticity and variable water density on tsunami speeds. Geophys. Res. Lett. 40 (3), 492–496.

Tsushima, H., Ohta, Y., 2014. Review on near-field tsunami forecasting from offshore tsunami data and onshore GNSS data for tsunami early warning. J. Disaster Res. 9 (3), 339–357.

Tsushima, H., Hino, R., Fujimoto, H., Tanioka, Y., Imamura, F., 2009. Near-field tsunami forecasting from cabled ocean bottom pressure data. J. Geophys. Res. Solid Earth 114. https://doi.org/10.1029/2008jb005988.

Tsushima, H., Hino, R., Tanioka, Y., Imamura, F., Fujimoto, H., 2012. Tsunami waveform inversion incorporating permanent seafloor deformation and its application to tsunami forecasting. J. Geophys. Res. 117, B03311. https://doi.org/10.1029/2011JB008877.

Ward, S.N., 1980. Relationships of tsunami generation and an earthquake source. J. Phys. Earth 28 (5), 441–474.

Watada, S., Kusumoto, S., Satake, K., 2014. Traveltime delay and initial phase reversal of distant tsunamis coupled with the self-gravitating elastic Earth. J. Geophys. Res. Solid Earth 119 (5), 4287–4310. https://doi.org/10.1002/2013jb010841.

Webb, S.C., 1998. Broadband seismology and noise under the ocean. Rev. Geophys. 36 (1), 105–142. https://doi.org/10.1029/97rg02287.

Yamamoto, T., 1982. Gravity waves and acoustic waves generated by submarine earthquakes. Soil Dyn. Earthq. Eng. 1 (2), 75–82.

Yamamoto, N., Aoi, S., Hirata, K., Suzuki, W., Kunugi, T., Nakamura, H., 2016. Multi-index method using offshore ocean-bottom pressure data for real-time tsunami forecast. Earth Planets Space 68 (1), 128. https://doi.org/10.1186/s40623-016-0500-7.

Yang, Y., Dunham, E.M., Barnier, G., Almquist, M., 2019. Tsunami wavefield reconstruction and forecasting using the ensemble Kalman filter. Geophys. Res. Lett. 46, 853–860. https://doi.org/10.1029/2018GL080644.